Available online at www.sciencedirect.com
ScienceDirect
Trans. Nonferrous Met. Soc. China 35(2025) 126−142
Transactions of Nonferrous Metals Society of China
www.tnmsc.cn

Prediction of microstructure evolution of ZK61 alloy during hot spinning by internal state variable model

Jin-qi PAN[1], Wen-cong ZHANG[1], Jian-lei YANG[1], Song-hui WANG[1], Yong WU[2], Huan LI[1]

1. School of Materials Science and Engineering, Harbin Institute of Technology Weihai, Weihai 264209, China;
2. College of Mechanical and Electrical Engineering, Nanjing University of Aeronautics and Astronautics, Nanjing 210016, China

Received 6 June 2023; accepted 30 January 2024

Abstract: An internal state variable (ISV) model was established according to the experimental results of hot plane strain compression (PSC) to predict the microstructure evolution during hot spinning of ZK61 alloy. The effects of the internal variables were considered in this ISV model, and the parameters were optimized by genetic algorithm. After validation, the ISV model was used to simulate the evolution of grain size (GS) and dynamic recrystallization (DRX) fraction during hot spinning via Abaqus and its subroutine Vumat. By comparing the simulated results with the experimental results, the application of the ISV model was proven to be reliable. Meanwhile, the strength of the thin-walled spun ZK61 tube increased from 303 to 334 MPa due to grain refinement by DRX and texture strengthening. Besides, some ultrafine grains (0.5 μm) that played an important role in mechanical properties were formed due to the proliferation, movement, and entanglement of dislocations during the spinning process.

Key words: internal state variable model; hot spinning; ZK61 alloy; finite element simulation; texture evolution

1 Introduction

Magnesium alloys are considered to be the most potential lightweight alloys in the field of aerospace because of their high specific strength and increasing demand for energy conservation [1]. However, the poor formability of magnesium alloys restricts their application, because only a few independent slip systems can be activated for the hexagonal close-packed (HCP) structure of magnesium at room temperature [2,3]. To overcome the poor formability, the methods of magnesium alloys processing are usually conducted at a temperature above 300 °C to activate more non-basal slip systems [4]. Moreover, dynamic recrystallization (DRX) usually occurs during the thermal plastic processing of magnesium alloys, which is beneficial to grain refinement and microstructure reconstruction [5]. Unfortunately, CHENG et al [6] pointed out that the softening mechanism was sensitive to the thermal processing parameters, indicating that the microstructure evolution could be optimized by controlling the deformation parameters.

At present, the constitutive modeling is significant to investigate the deformation characteristics of materials during the thermal processing [7,8]. Numerous studies have been conducted to reveal the flow behavior of the materials using the Johnson−Cook model [9] and the Arrhenius model [10]. However, these phenomenological models always take temperature, strain, and strain rate as variables, which makes it hard to reveal the physical insight of the material. In contrast, physically-based models that involve

Corresponding author: Jian-lei YANG, Tel: +86-631-5672167, E-mail: jlyang@hit.edu.cn
https://doi.org/10.1016/S1003-6326(24)66669-0

internal state variables (ISV) can be applied to revealing the evolution of the grain size (GS) and DRX fraction as well as dislocation density. Moreover, the ISV model can accurately describe the microstructure and has been conducted to predict the microstructure evolution on a finite element (FE) platform. HUO et al [11] applied the ISV model to cross wedge rolling of 25CrMo4 steel and well predicted the GS and recrystallization fraction. ALABORT et al [12] established the physically-based ISV model to study the evolution of GS, void fraction, and dislocation density of Ti64 alloy during superplastic forming. The results showed that the FE results well matched the test results, which confirmed the accuracy of the ISV model.

Since the microstructure of magnesium alloys is hard to control during thermal plastic working, applying a physically-based ISV model to FE is a useful method of simulating the microstructure evolution to optimize the deformation conditions. XU et al [13] imported the ISV model into FE analysis of hot extrusion of the Mg−Gd−Y−Zr alloy and successfully predicted the GS and DRX distribution, which provided guidance for the thermal processing of magnesium alloys. In the study of SU et al [14], the unified ISV model was verified and embedded in FE software to simulate the ECAE (equal channel angular extrusion) of AZ80 alloy. The experimental results proved that the ISV model could provide a reliable prediction for the thermal plastic processing of AZ80 alloy. JIN et al [15] and CAO et al [16] demonstrated that cracks easily occurred during hot spinning due to the difficulty in controlling the microstructure of magnesium alloys. To enhance the plastic forming capability of magnesium alloys, it is significant to predict the microstructure evolution of hot spinning via the ISV model.

In the present study, an ISV model was established based on the results of the ZK61 alloy during hot plane strain compression (PSC), and its reliability was verified by comparing the flow stress, GS, and DRX fractions. Next, ISV model was used to simulate the microstructure evolution of the hot spinning process, and its reliability was verified. Finally, the formation mechanism of the ultrafine grains was present, and the strengthening mechanisms of the spun alloys were revealed. This study may provide an efficacious solution for the thermal processing of magnesium alloys in predicting the microstructure evolution.

2 Experimental

2.1 PSC tests

The initial material was Mg−6.03wt.%Zn−0.55wt.%Zr alloy (ZK61) extruded tube, which was extruded at 450 °C with an extrusion speed of 0.3 mm/s. The hot PSC experiments were carried out by a Gleeble−3500 machine with temperatures ranging from 300 to 500 °C and strain rates ranging from 0.01 to 10 s^{-1}. To investigate the microstructure evolution and deformation mechanism as a function of strain, some hot PSC samples were tested with true strains of 0.26, 0.59, and 1.06, respectively. The PSC samples were cut from the center of the extruded ZK61 tube (RD: radial direction, ED: extrusion direction, TD: transverse direction) with a dimension of 10 mm (RD) × 15 mm (ED) × 20 mm (TD). Figure 1 shows the schematic diagram and dimension of the hot PSC sample. The testing plane was the ED−TD plane and the compression direction (CD) was RD. After the tests were completed, the samples were cooled with water to maintain the hot PSCed microstructure.

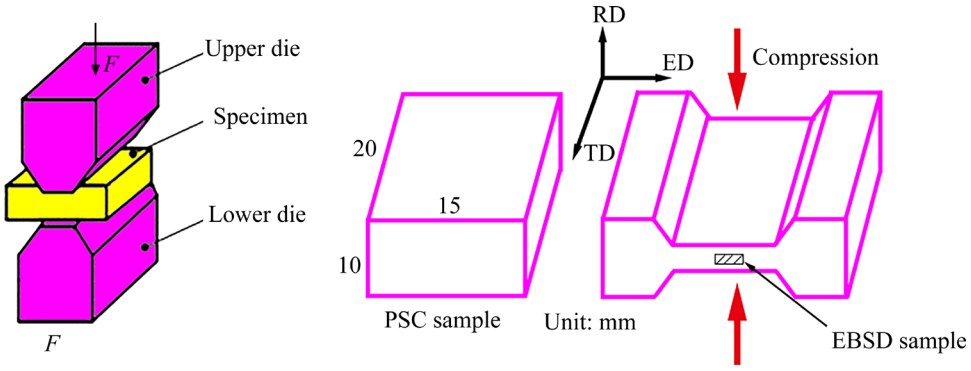

Fig. 1 Schematic diagram and dimension of hot PSC sample

2.2 Hot spinning experiment

Figure 2(a) shows the hot spinning process of ZK61 extruded tube conducted on the SXY−800 spinning machine, which was made in Bosai CNC Machine Tools Co., China. The mandrel rotation speed and the roller feed rate were 200 r/min and 75 mm/min, respectively. Figure 2(b) shows the original extruded tube and spun tube. The extruded tube was 165 mm in outer diameter and 10 mm in thickness. Before the spinning experiment, the extruded tube was heated to 350 °C in the furnace and then kept at this temperature for 30 min to ensure a uniform temperature throughout the tube. Moreover, the mandrel and the rollers were pre-heated to 200 °C using the spray gun to prevent temperature drop of the tube. The spinning process was divided into six passes and the thickness reduction of each pass was presented in Table 1. After the hot spinning experiment, a spun tube with 1.4 mm in thickness was successfully obtained.

2.3 Microstructure characterization

The microstructure of the ZK61 alloy was characterized by an optical microscope (OM), a scanning electron microscope (SEM, Zeiss) equipped with electron backscattered diffraction (EBSD), and a transmission electron microscope (TEM). The OM specimens were corroded in a solution of 0.8 g $C_6H_3N_3O_7$ + 4 mL CH_3COOH + 4 mL H_2O + 10 mL C_2H_5OH for 6−8 s. For the EBSD test, the specimens were mechanically polished with sandpaper and then electrolytically polished in an ethanol and phosphoric acid (5:3) solution with a current of 0.5 A for 2 min. The EBSD test was conducted at a voltage of 20 kV. The TEM samples were prepared on a Gatan 691 ion beam thinner and then detected with a voltage of 200 kV.

3 Model establishment and validation

3.1 Establishment of ISV model

Based on Hooke's law, YASMEEN et al [17] expressed the true stress−strain relation as

$$\sigma=E(\varepsilon_T-\varepsilon_P) \tag{1}$$

where E is the elastic modulus, ε_T and ε_P are total strain and plastic strain, respectively, and σ is the flow stress.

The hyperbolic-sine type flow equation can be introduced to characterize the relationship between flow stress and microstructure characteristics under various deformation conditions in LIN's study [18]:

$$\dot{\varepsilon}_p=\left(\frac{d_0}{d}\right)^{\mu}\left(\frac{\sigma-\sigma_0-H}{K}\right)^{n} \tag{2}$$

where K is material constants, $\dot{\varepsilon}_p$ is the strain rate, σ_0 is the yield stress, d and d_0 are the GS and initial GS, μ represents the GS parameter, and n represents the index of stress parameter.

The hardening variable H of the material during plastic deformation is related to the dislocation density ρ. The hardening stress in Eq. (2) can be expressed as [19]

$$H=B\bar{\rho}^{0.5} \tag{3}$$

where B is a temperature-dependent parameter of the material, and $\bar{\rho}$ is normalized dislocation density. It can be simplified as $\bar{\rho}=1-\rho_0/\rho$ [20] where ρ_0 and ρ are the initial and deformed dislocation density. The value of $\bar{\rho}$ is in the range of 0−1.

LIN and DEAN [21] suggested that the dislocation density ($\dot{\bar{\rho}}$) was regarded as an internal parameter of the material and it could be quantified as

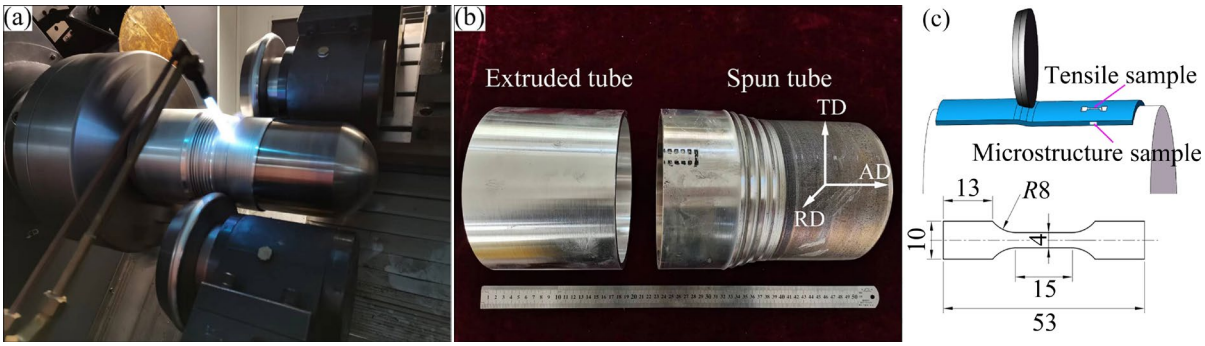

Fig. 2 Hot spinning experiment: (a) Hot spinning process; (b) Tubular workpiece; (c) Dimension of samples (Unit: mm)

Table 1 Thickness reduction of ZK61 tube under different passes

Pass No.	Wall thickness/mm	Total thickness reduction/%
0	10	0
1	7.5	25
2	6.3	37
3	4.9	51
4	3.3	67
5	2.5	75
6	1.4	86

$$\dot{\overline{\rho}} = A\dot{\varepsilon}_{\mathrm{p}}^{\delta}\cdot|\dot{\varepsilon}_{\mathrm{p}}| - k_1\overline{\rho}\dot{\varepsilon}_{\mathrm{p}}^{\delta_1}|\dot{\varepsilon}_{\mathrm{p}}| - k_2\overline{\rho}^{\delta_2} - k_3\overline{\rho}\frac{\dot{S}}{1-S} \tag{4}$$

where A, k_1, k_2, k_3, δ_1 and δ_2 are temperature-dependent parameters of the material. The first item reveals the dislocation storage induced by plastic strain. The second and third items are the reduced dislocation density caused by dynamic recovery and static recovery. The final item is to explain the reduction in dislocation density due to dynamic recrystallization (DRX), and the S represents the fraction of DRXed grains.

During the plastic deformation of materials, the material will undergo a DRX process when the temperature exceeds recrystallization temperature. The occurrence of DRX will consume a large amount of the generated dislocations during the plastic deformation. In the work of JI et al [22], the rate of DRX ($\dot{S}$) is defined as

$$\dot{S} = q_1\left[x\overline{\rho} - \overline{\rho}_{\mathrm{c}}(1-S)\right](1-S)^{q_2}\dot{\varepsilon}^{q_3}/\overline{d} \tag{5}$$

$$\dot{x} = A_0(1-x)\overline{\rho} \tag{6}$$

where x is put forward to represent in cubation fraction. A_0, q_1, q_2 and q_3 are temperature-dependent parameters of the material.

In the work of CHO et al [23], the sub-grains grow through aggregation and annexation of the surrounding smaller sub-grains driven by the thermal effect during plastic deformation, and the plastic deformation-induced grain growth rate ($\dot{d}_1$) can be expressed as

$$\dot{d}_1 = \alpha_1 d^{-\gamma_1} \tag{7}$$

α_1 in Eq. (7) is given by $\alpha_1=M_{\mathrm{b}}\sigma_{\mathrm{surf}}$, where M_{b} and σ_{surf} represent the mobility and energy density of the grain boundary, respectively. The static grain growth rate is considered to be an atomic diffusion process influenced by temperature, which is related to the mobility and energy density of the grain boundary. SANDSTRÖM and LAGNEBORG [24] proposed that the static grain growth rate ($\dot{d}_2$) was characterized by

$$\dot{d}_2 = \alpha_2\dot{\varepsilon}_{\mathrm{p}}d^{-\gamma_2} \tag{8}$$

where α_2, γ_1 and γ_2 are temperature-dependent parameters of the material.

In the study of LIN and LIU [25], the DRX behavior of the material during plastic deformation at high temperatures will promote the size change, and the resulting GS change rate ($\dot{d}_3$) is simplified as

$$\dot{d}_3 = -\alpha_3\dot{S}^{\gamma_3}d^{\gamma_4} \tag{9}$$

where α_3, γ_3 and γ_4 are temperature-dependent parameters of the material.

After comprehensive consideration of the effects of static grain growth, plastic deformation-induced grain growth, and dynamic recrystallization behavior on GS, the relative GS change rate of the material ($\dot{\overline{d}}$) can be expressed as

$$\dot{\overline{d}} = \alpha_1 d^{-\gamma_1} + \alpha_2\dot{\varepsilon}_{\mathrm{p}}d^{-\gamma_2} - \alpha_3\dot{S}^{\gamma_3}d^{\gamma_4} \tag{10}$$

During plastic deformation, distortion energy and thermal energy occur within the material. Most of the energy is converted into heat, leading to an increase in the temperature of the material, which in turn affects the dislocation density, recrystallization ratio, grain size, etc., and reduces the plastic deformation resistance of the material. The effect of plastic deformation on the material temperature can be expressed as

$$\Delta T = \frac{\eta}{C_V d_{\mathrm{n}}}\int_0^{\varepsilon_{\mathrm{p}}}\sigma\mathrm{d}\varepsilon_{\mathrm{p}} \tag{11}$$

where η, C_V and d_{n} are heat dissipation fraction (0.9), specific heat capacity and density of the material, respectively.

Therefore, the constitutive equations are as follows:

$$\dot{\varepsilon}_{\mathrm{p}} = \left(\frac{d_0}{d}\right)^{\mu}\left(\frac{\sigma-\sigma_0-H}{K}\right)^{n}$$

$$H = B\overline{\rho}^{0.5}$$

$$\dot{S} = q_1\left[x\overline{\rho} - \overline{\rho}_{\mathrm{c}}(1-S)\right](1-S)^{q_2}\dot{\varepsilon}^{q_3}/\overline{d}$$

$$\dot{\overline{\rho}} = A\dot{\varepsilon}_{\mathrm{p}}^{\delta}\cdot|\dot{\varepsilon}_{\mathrm{p}}| - k_1\overline{\rho}\dot{\varepsilon}_{\mathrm{p}}^{\delta_1}|\dot{\varepsilon}_{\mathrm{p}}| - k_2\overline{\rho}^{\delta_2} - k_3\overline{\rho}\frac{\dot{S}}{1-S}$$

$$\dot{x} = A_0(1-x)\overline{\rho}$$

$$\dot{\overline{d}} = \alpha_1 d^{-\gamma_1} + \alpha_2 \dot{\varepsilon}_p d^{-\gamma_2} - \alpha_3 \dot{S}^{\gamma_3} d^{\gamma_4}$$

The corresponding parameters of the material in the constitutive equations took the form of Arrhenius equations and were calculated using the genetic algorithm optimization method, as shown in Fig. 3, Tables 2 and 3.

3.2 Validation of ISV model

Figure 4 presents the comparison between the true stress−strain curves and the calculated results using the ISV model of the ZK61 alloy during hot PSC at strain rates of 10, 1, 0.1 and 0.01 s^{-1}. It was found that most of the calculated results of the ISV model were consistent with experimental results, while part of the flow stress deviated slightly from the fitting curve at 300 °C which might be attributed to the dynamic balance between the work hardening and the thermal softening at low temperatures. These results revealed the fact that the ISV model could predict the work hardening and thermal softening trends of the ZK61 alloy.

To verify the microstructure evolution during the PSC, Fig. 5 exhibits the inverse pole figure (IPF) maps of the extruded (Fig. 5(a)) and hot PSC specimens deformed at 450 °C and 1 s^{-1} with the true strains of 0.26, 0.59, and 1.06, respectively (Figs. 5(b−d)). The extruded ZK61 alloy consisted of equiaxed grains and some un-extruded grains with a mean diameter (d_m) of 31.62 μm. At a low strain of 0.26 as shown in Fig. 5(b), the microstructure consisted of DRX grains and initial large grains whose d_m was 24.2 μm. As the

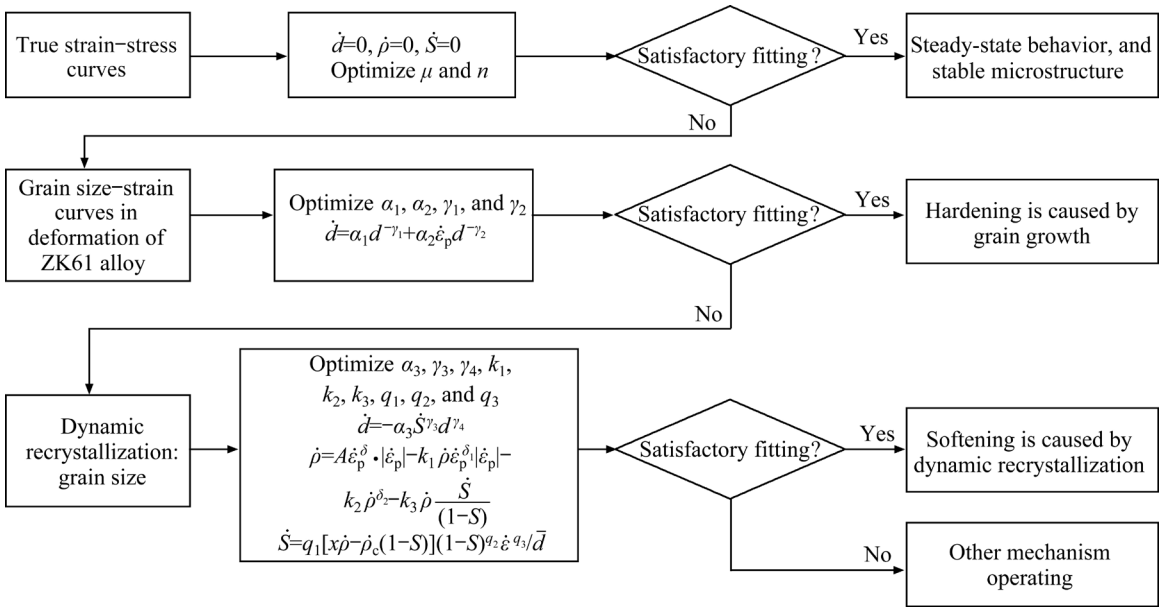

Fig. 3 Genetic algorithm optimization method of ISV parameters

Table 2 Temperature-dependent parameters of material

Equation	Equation	Equation
$\sigma_0=\sigma_{0,0}\exp[Q_{\sigma 0}/(RT)]$	$q_2=q_{2,0}\exp[-Q_{q2}/(RT)]$	$\alpha_1=\alpha_{1,0}\exp[-Q_{\alpha 1}/(RT)]$
$E=E_0\exp[Q_E/(RT)]$	$q_3=q_{3,0}\exp[Q_{q3}/(RT)]$	$\alpha_2=\alpha_{2,0}\exp[-Q_{\alpha 2}/(RT)]$
$K=K_0\exp[Q_K/(RT)]$	$A=A_0\exp[Q_A/(RT)]$	$\alpha_3=\alpha_{3,0}\exp[Q_{\alpha 3}/(RT)]$
$n=n_0\exp[Q_n/(RT)]$	$\delta=\delta_0\exp[-Q_\delta/(RT)]$	$\gamma_1=\gamma_{1,0}\exp[-Q_{\gamma 1}/(RT)]$
$\mu=\mu_0\exp[Q_\mu/(RT)]$	$\delta_1=\delta_{1,0}\exp[-Q_{\delta 1}/(RT)]$	$\gamma_2=\gamma_{2,0}\exp[Q_{\gamma 2}/(RT)]$
$d_1=d_{1,0}\exp[Q_{d1}/(RT)]$	$\delta_2=\delta_{2,0}\exp[Q_{\delta 2}/(RT)]$	$\gamma_3=\gamma_{3,0}\exp[Q_{\gamma 3}/(RT)]$
$d_2=d_{2,0}\exp[-Q_{d2}/(RT)]$	$k_1=k_{1,0}\exp[Q_{k1}/(RT)]$	$\gamma_4=\gamma_{4,0}\exp[Q_{\gamma 4}/(RT)]$
$B=B_0\exp[Q_B/(RT)]$	$k_2=k_{2,0}\exp[Q_{k2}/(RT)]$	
$q_1=q_{1,0}\exp[Q_{q1}/(RT)]$	$k_3=k_{3,0}\exp[-Q_{k3}/(RT)]$	

Table 3 Determined constants in unified constitution equations

Material constant	Value	Material constant	Value	Material constant	Value
E_0/MPa	2.553×10^4	Q_{q1}/(J·mol^{-1})	6.6758×10^3	$k_{3,0}$	2.02342×10^{-4}
Q_E/(J·mol^{-1})	6.12925×10^4	$q_{2,0}$	1.62005	Q_{k3}/(J·mol^{-1})	3.7871×10^4
$\sigma_{0,0}$	9.834×10^{-6}	Q_{q2}/(J·mol^{-1})	3.5198×10^2	$\alpha_{1,0}$	2.71×10^{-2}
$Q_{\sigma0}$/(J·mol^{-1})	6.682×10^4	$q_{3,0}$	8.8261×10^{-1}	$Q_{\alpha1}$/(J·mol^{-1})	3.56125×10^4
K_0	1.32834	Q_{q3}/(J·mol^{-1})	2.001×10^2	$\alpha_{2,0}$	3.091×10^{-2}
Q_K/(J·mol^{-1})	1.8243×10^4	A_0	1.601×10^{-2}	$Q_{\alpha2}$/(J·mol^{-1})	5.00182×10^3
n_0	1.83321	Q_A/(J·mol^{-1})	3.8603×10^4	$\alpha_{3,0}$	1.641×10^{-1}
Q_n/(J·mol^{-1})	3.14762×10^3	δ_0	2.12126	$Q_{\alpha3}$/(J·mol^{-1})	8.83044×10^3
μ_0	4.12792	Q_δ/(J·mol^{-1})	1.403×10^4	$\gamma_{1,0}$	9.801×10^{-1}
Q_μ/(J·mol^{-1})	6.399×10^3	$\delta_{1,0}$	3.13641	$Q_{\gamma1}$/(J·mol^{-1})	7.0281×10^2
$B_{0,0}$	0.51237	$Q_{\delta1}$/(J·mol^{-1})	1.134×10^4	$\gamma_{2,0}$	2.0688
Q_{B0}/(J·mol^{-1})	2.5692×10^4	$\delta_{2,0}$	2.34017	$Q_{\gamma2}$/(J·mol^{-1})	5.34039×10^1
$d_{1,0}$	1.12403	$Q_{\delta2}$/(J·mol^{-1})	1.661×10^3	$\gamma_{3,0}$	1.00213
Q_{d1}/(J·mol^{-1})	7.0012×10^2	$k_{1,0}$	5.69003	$Q_{\gamma3}$/(J·mol^{-1})	6.7784×10^1
$d_{2,0}$	2.50112	Q_{k1}/(J·mol^{-1})	8.0202×10^3	$\gamma_{4,0}$	1.1801×10^{-1}
Q_{d2}/(J·mol^{-1})	3.2365×10^3	$k_{2,0}$	2.31376	$Q_{\gamma4}$	8.27034×10^1
$q_{1,0}$	8.4393×10^{-1}	Q_{k2}/(J·mol^{-1})	4.1128×10^4		

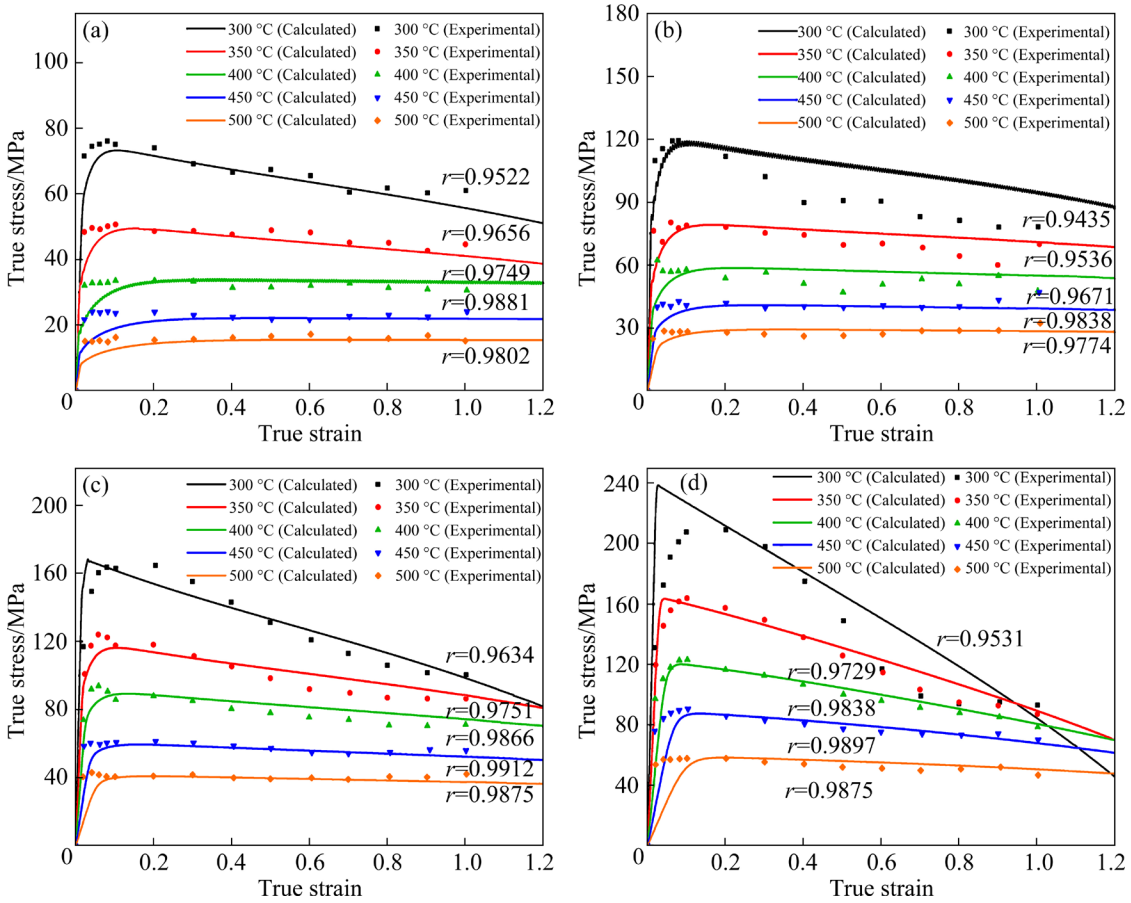

Fig. 4 Comparison between prediction results of ISV and true stress−strain curves during high temperature plane strain compression: (a) 0.01 s^{-1}; (b) 0.1 s^{-1}; (c) 1 s^{-1}; (d) 10 s^{-1}

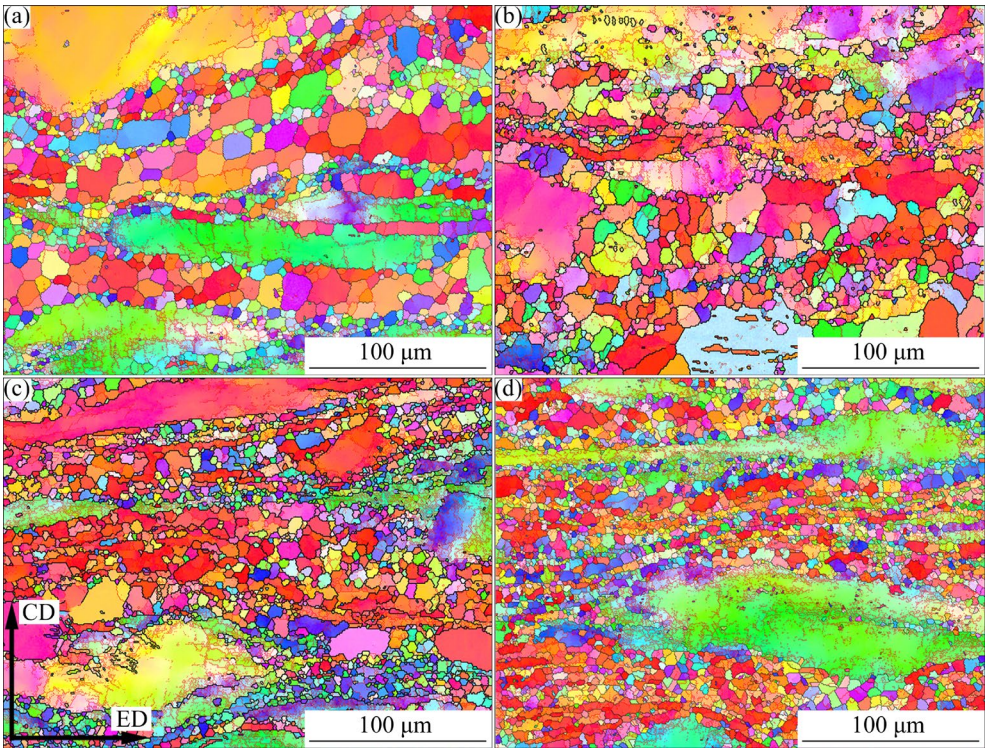

Fig. 5 IPF maps of extruded (a) and hot PSC specimens deformed at 450 °C and 1 s^{-1} with true strains of 0.26 (b), 0.59 (c) and 1.06 (d)

deformation proceeded, the microstructure showed a "necklace" structure that consisted of fine DRX grains, and the grain refinement effect was more pronounced. The comparison between the calculated GS results and the experimental GS results at 450 °C during the PSC is presented in Fig. 6. The calculated results showed that the GS decreased rapidly and then tended to be stable. The experimental GS matched well with the calculated results, where the correlation coefficient (r) was 0.9968.

To better verify the DRX fraction during the hot PSC, the grain orientation spread (GOS) value distributions under different strains were calculated, as shown in Fig. 7. The GOS value was used to evaluate the average misorientations of the surrounding pixel points, and grains with a GOS value lower than 2 were considered DRXed grains (marked in blue). It was shown that the DRX fraction increased from 38.7% to 51.5% as the strain increased from 0.26 to 1.06, indicating that the severe plastic deformation promoted the DRX process due to more lattice distortion energy and sufficient DRX time. With the proceeding of hot PSC, more extruded coarse grains (in red) experienced plastic deformation, and occurred during

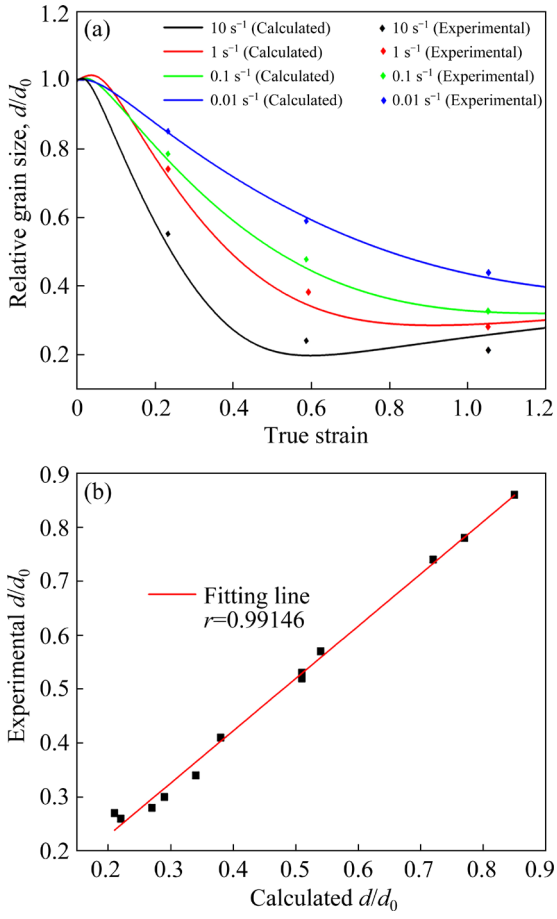

Fig. 6 Plots of calculated GS results (a) and fitting results (b) at 450 °C

the DRX process, resulting in a large decrease in the lattice distortion energy. The comparison between the calculated DRX fractions and the experimental DRX fractions under various deformation conditions is presented in Fig. 8. The experimental results matched the calculated ones with a relatively low deviation, indicating that the ISV model could be used to predict microstructure evolution.

4 Results and discussion

4.1 Microstructure prediction during hot spinning using ISV model

4.1.1 FE simulation of hot spinning

In the process of power spinning the tube workpiece, compression deformation occurred in the radial direction (RD) and tensile deformation occurred in the axial direction (AD), while the flow of material in the TD was hindered. Based on the ISV constitutive model during hot PSC, this study simulated the hot spinning of the ZK61 alloy via the FE software Abaqus and its subroutine Vumat, which coupled the fields of heat, stress, and microstructure to reflect the microstructure evolution during hot spinning. The FE model of the ZK61 alloy is presented in Fig. 9. The element mesh of the deformable workpiece was set to be C3D8R [26]. The friction coefficient between dies and workpiece was set at 0.15 using the Coulomb friction model [27,28]. The spinning process was divided into three passes, and the thickness reduction was 10, 7, 5 and 4 mm at 350 °C. The spinning rotational speed of the mandrel

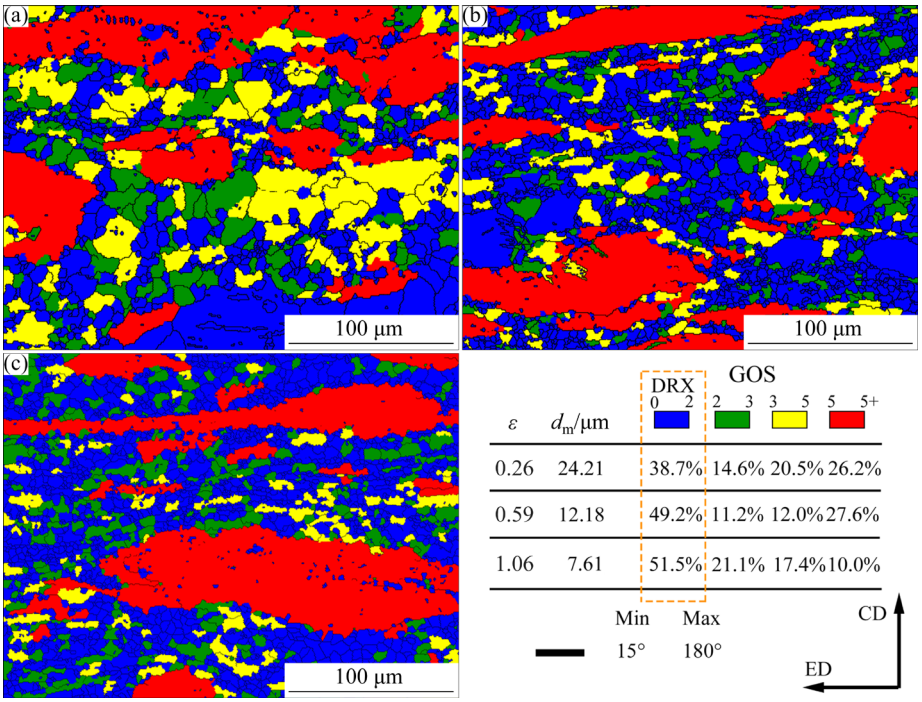

Fig. 7 GOS distributions of hot PSC specimens deformed at 450 °C and 1 s^{-1} with true strains of 0.26 (a), 0.59 (b) and 1.06 (c)

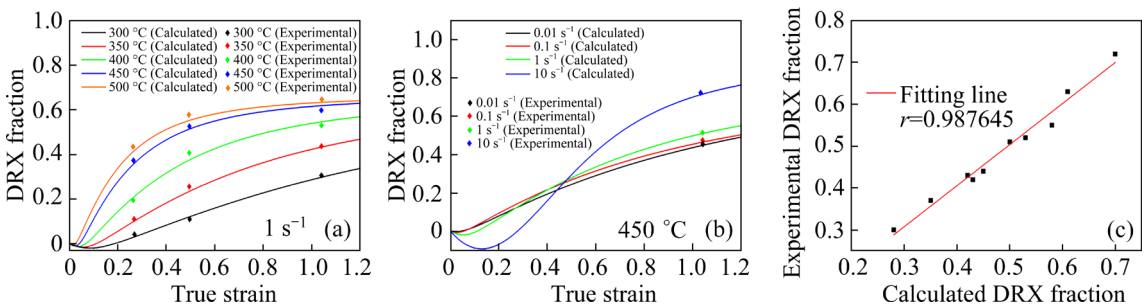

Fig. 8 Comparison between calculated DRX fraction and experimental DRX fraction at 1 s^{-1} (a) and 450 °C (b), and fitting result (c)

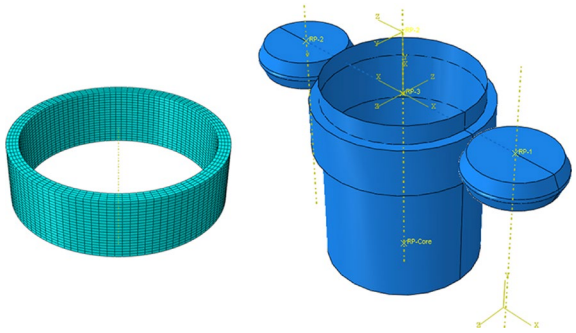

Fig. 9 FE model of ZK61 alloy during hot spinning

was set at 200 r/min, and the feed rate of the rollers along AD was 75 mm/min.

4.1.2 ISV distribution of hot spinning

Figure 10 shows the simulated ISV distribution of the relative GS and the DRX fraction after different passes of hot spinning. At the beginning of spinning (Pass 0), the rollers were embedded in the workpiece, and the deformation was mainly concentrated in the contact area between the rollers and the workpiece. From Figs. 10(a, b), the grains in the contact area were partially refined due to the DRX process, while the DRX did not occur in the un-deformed area. As shown in Figs. 10(c, d), when the first pass of spinning was completed, the GS of the outer layer material was about 46% that of the initial grain, and the DRX fraction was as high as

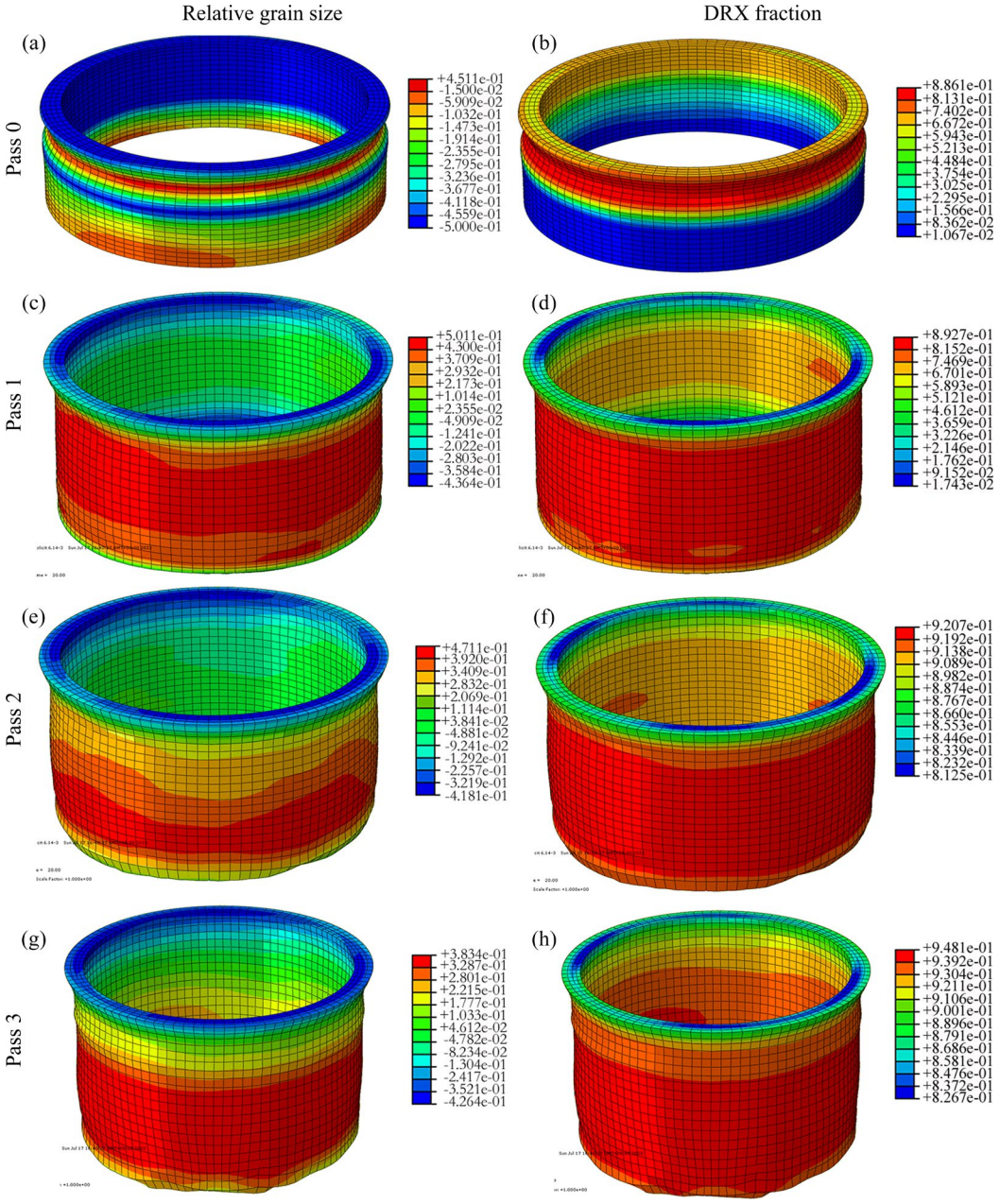

Fig. 10 Simulated distributions of relative GS (a, c, e, g) and DRX fraction (b, d, f, h) during hot spinning

89%. However, the DRX fraction of the inner layer was at a lower degree of DRX due to the smaller amount of plastic deformation. As shown in Figs. 10(e, f), after two passes of spinning, the grains were further refined, but at a reduced rate due to the constant heating of the spray gun, while the DRX fraction was nearly stabilized. When the third pass of spinning was completed, the GS distribution on the outer surface of the tube was uniform, and the maximum DRX fraction reached 94%, indicating that the DRX process was nearly complete.

4.2 Microstructure characteristics during hot spinning

Figure 11 shows the microstructure of the ZK61 alloy after different hot spinning passes. From Figs. 11(a, b), the coarse grains in the extruded tube were greatly refined with some aggregate colonies of fine grains after 1 pass of spinning. With increasing the hot spinning passes, as shown in Figs. 11(c−g), the aggregate colonies of fine grains gradually combined and formed strip-like structures. After 6 passes of spinning, the microstructure was composed of stripe-like ultrafine grains aggregation and equiaxed DRXed grains, which was consistent with the report of XIA et al [29].

To validate the reliability of the ISV model in predicting the GS during the hot spinning process, the simulated distribution of GS using the ISV model and the experimental results are presented in Fig. 11(h). The experimental GS was calculated by Nano Measurer software, and the simulated results were calculated by Abaqus software. As shown in Fig. 11(h), the GS was rapidly refined from 32.4 to 15.1 μm after 1 pass of spinning and then gradually refined as the spinning pass increased. The comparison between the simulated and experimental results indicated the reliability of the ISV model in predicting the GS evolution during the hot spinning process.

Figure 12 presents the GOS distributions after 1 pass and 6 passes of hot spinning. The GOS value lower than 2 (in blue) was considered to be DRXed grains. From Fig. 12(a), the DRX fraction could reach 87.3% after 1 pass of spinning. With the strain accumulation during hot spinning, the DRX fraction gradually increased. After 6 passes of spinning, the DRX fraction was 95.3%, indicating that the DRX process was nearly complete. Compared with hot PSC, the DRX fractions of hot spinning were much higher owing to the larger plastic deformation of the material at the same thickness reduction during the spinning process. Under the driving force of the rollers, the outer surface material of the ZK61 tube continuously took part in plastic deformation under the compression of the surrounding material and the rollers, resulting in a nearly complete DRX process during hot spinning.

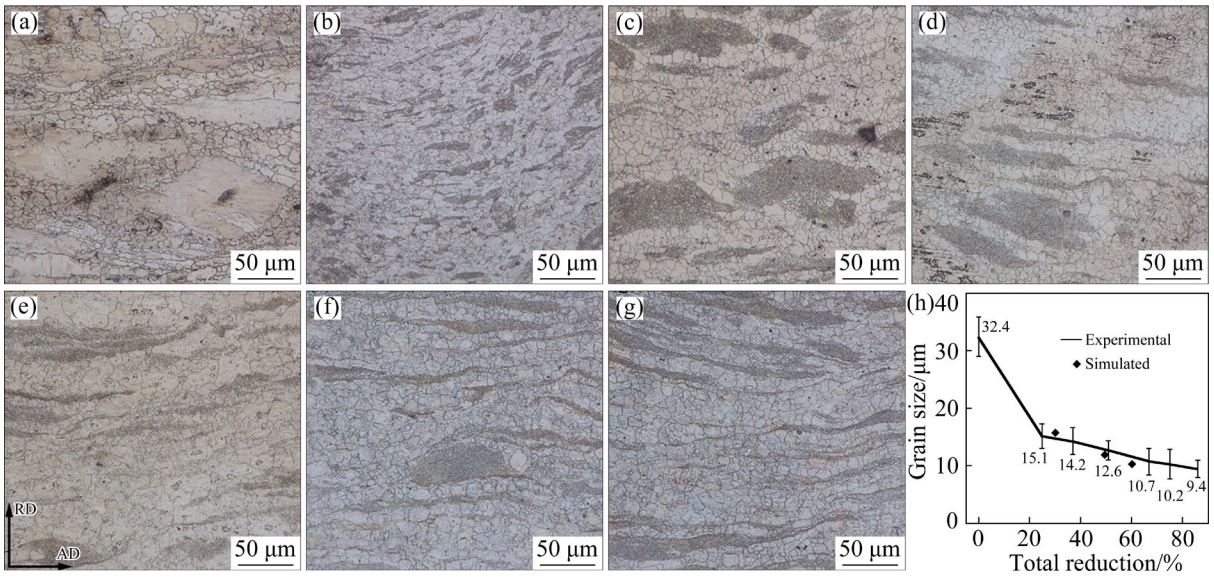

Fig. 11 Microstructures of ZK61 alloy after different hot spinning passes: (a) Original microstructure (reduction 0%); (b) 1 pass (reduction 25%); (c) 2 passes (reduction 37%); (d) 3 passes (reduction 51%); (e) 4 passes (reduction 67%); (f) 5 passes (reduction 75%); (g) 6 passes (reduction 86%); (h) GS validation result

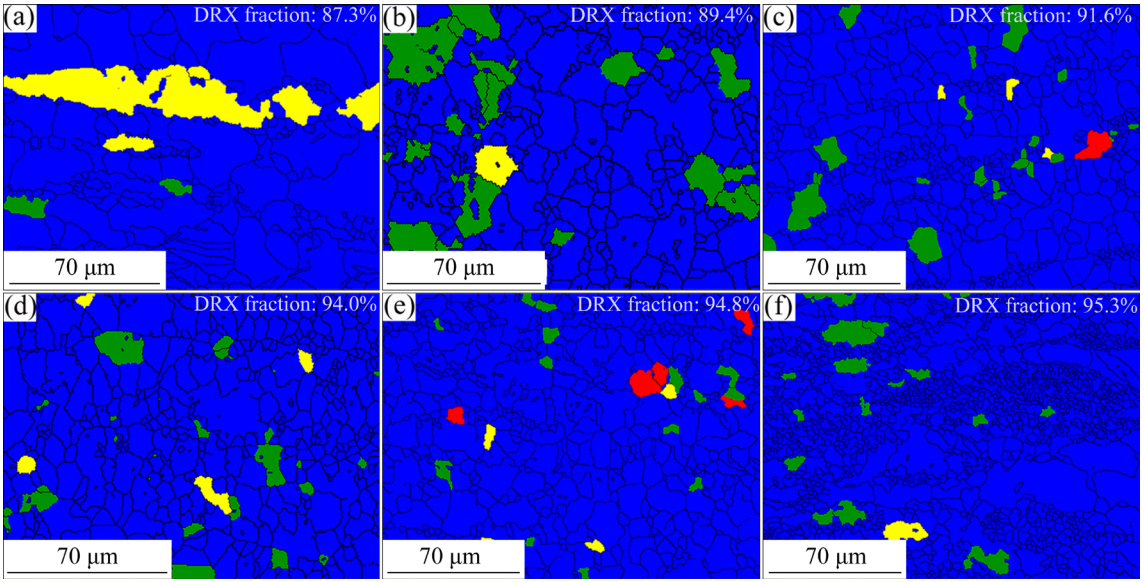

Fig. 12 GOS distributions of ZK61 alloy after different passes of spinning: (a) 1; (b) 2; (c) 3; (d) 4; (e) 5; (f) 6

Figure 13 depicts the simulated and experimental DRX fractions under different total thickness reductions of spinning. The DRX fractions were all at a high level during the hot spinning process. Moreover, the simulated values based on the ISV model matched well with the experimental values with little deviation, indicating that the ISV model was reliable in predicting the DRX process during hot spinning.

In the process of hot spinning, the grains rotated due to the activation of slip systems, and the basal texture was susceptible to forming. Figure 14 shows the texture evolution during hot spinning. The as-extruded ZK61 alloys presented a fiber (0002) texture where the *c*-axes of the grains were perpendicular to AD and were randomly distributed in RD (Fig. 14(a)). After 1 pass of spinning, the (0002) basal still presented a fiber state, but the *c*-axes of the grains were slightly deflected in AD with an angle of ~10° (Fig. 14(b)). Moreover, the maximum intensity increased from 5.81 to 10.24. With the spinning pass increased, the (0002) fiber texture was replaced by plane texture with the maximum intensity increasing to 15.44 (Fig. 14(c)). After 6 passes of spinning, the basal texture became more concentrated and the texture maximum intensity increased to 19.72, indicating that the spinning process greatly modified the grain orientation and most of the grains shared the same orientation (Fig. 14(d)). Compared with the (0002) texture, there was no significant change in the

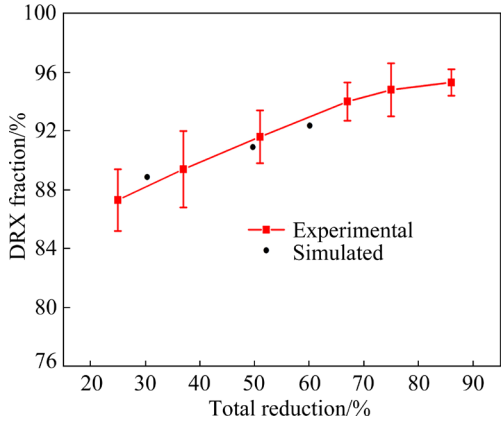

Fig. 13 Experimental and simulated DRX fraction during hot spinning

$(11\bar{2}0)$ and $(10\bar{1}0)$ textures except for a certain angular deflection, and $(11\bar{2}0)$ and $(10\bar{1}0)$ textures were randomly distributed along AD.

Figure 15 shows the forces during the spinning process. Spinning workpieces within the forming area were subjected to different stresses in three main directions: the compressive stress in the radial direction (F_R), the shear stress in the axial direction (F_A) and the circumferential stress in the tangential direction (F_T). The tilt of the grains was related to the combined force of F_R and F_A that caused the shear deformation in the AD. As reported, the shear strain could promote the rotation of the grains to form a tilted texture component in Mg alloy [30,31]. After spinning, the grains exhibited the preferred orientation and their schematic diagram is shown in Fig. 15.

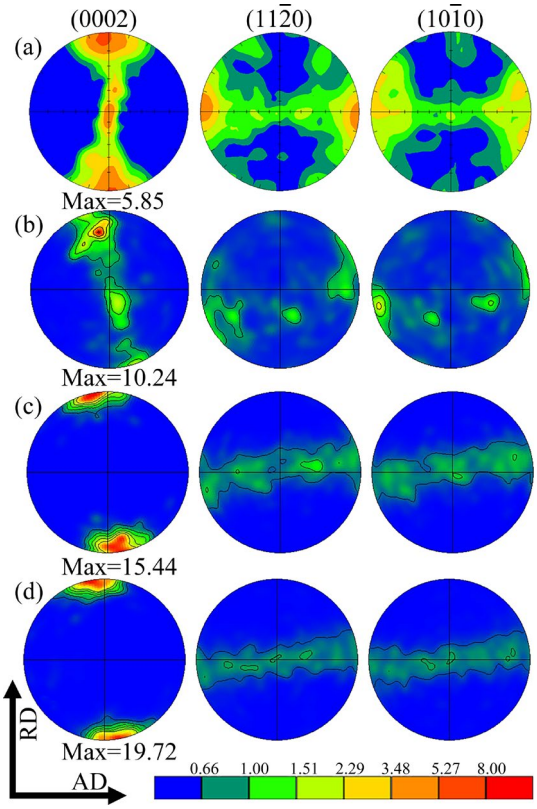

Fig. 14 Texture evolution during hot spinning: (a) Extruded texture; (b) After 1 pass; (c) After 3 passes; (d) After 6 passes

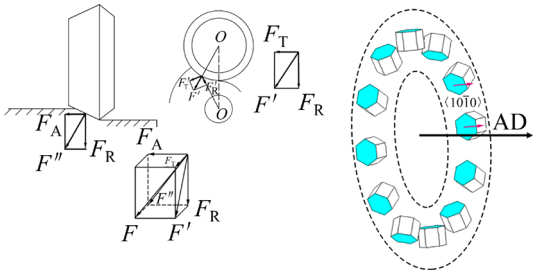

Fig. 15 Diagram of forces and grain orientation of ZK61 tube during spinning

4.3 Formation mechanism of ultrafine grains

Figure 16 shows the SEM images of the spun ZK61 alloy. In addition to a large number of equiaxed DRXed grains, some of the deformed grains were replaced by ultrafine grain aggregation. Figure 16(b) presents the magnified microstructure of the grain aggregation and the aggregate colonies consisting of ultrafine grains with a d_m of 0.5 μm which were generated by the uneven plastic deformation during hot spinning.

Figure 17 shows the TEM images of the spun ZK61 alloy after hot spinning. During the spinning process, the outer surface material was subjected to plastic deformation by the action of the spinning pressure, which was manifested on a microscopic scale by proliferation, movement and entanglement of dislocations, as shown in Fig. 17(a). As a result, the dislocation wall was formed, which refined the original grains into a cellular shape. To reduce the stored energy, dislocations were entangled in each other to form dislocation interfaces by climbing. However, the dislocation climbing was hindered at the grain boundaries, which restricted the dislocation movement to nearby grains. The dislocation interfaces were divided into geometrically necessary boundaries (GNDs) and incidental dislocation boundaries (IDBs). The GNDs were relatively straight and had some macroscopic orientation. With the increase of the spinning passes, thin lamellar boundaries that were parallel to the AD could be observed in the microstructure, as can be seen in Fig. 11. The fragmentation of the coarse grains into ultrafine subgrains was necessary for the coordination of deformation and the boundaries of the subgrains were GNDs (Fig. 17(d)). The IDBs were mainly the walls of the dislocation cells, which were caused by the interaction of dislocations during the hot spinning.

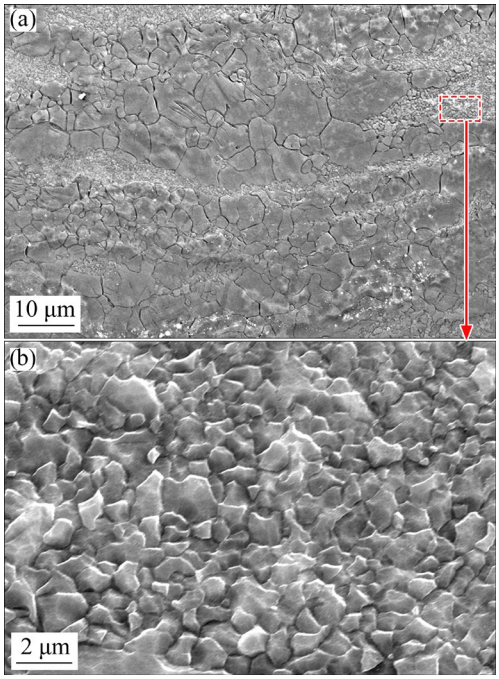

Fig. 16 SEM images of spun ZK61 alloy: (a) In low magnification; (b) In high magnification

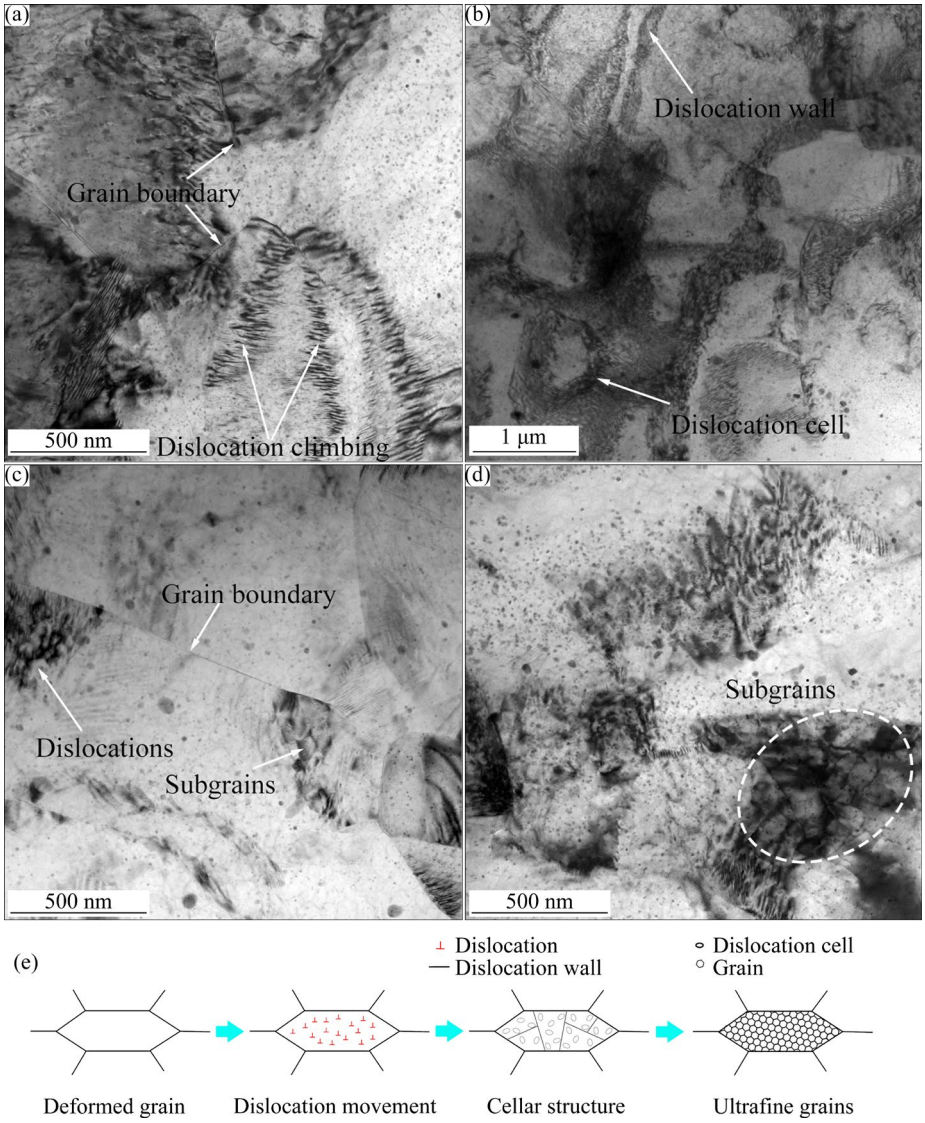

Fig. 17 TEM images of spun alloy (a−d) and formation schematic diagram of ultrafine grains (e)

From Fig. 17(b), the dislocation density within the dislocation cells was low, indicating that the formation of cellar structures was the result of the low energy dislocations. Moreover, the dislocations were randomly distributed in the cell wall and the slips within the cell were similar for all dislocated cellular structures, so the orientation differences between cellular structures were small. As the strain accumulated, the dislocation density in the cell wall increased to such an extent that the dislocation slips of each cell within the coarse grains were no longer the same and they became new cells. Therefore, the cell wall changed from IDBs to GNBs, which greatly refined the coarse grains.

Figure 17(e) shows the formation diagram of the ultrafine grains within the coarse deformed grains. At the beginning of spinning, the differences in the activation of deformation slips in various regions of the grain led to grain fragmentation. The fragmentation of the regions was separated by dislocation walls. As the hot spinning proceeded, the dislocation density inside the dislocation wall increased further and dislocation cells were formed. The cellar structure continued to proliferate, and the cell walls transformed into grain boundaries as the spinning passes increased. Finally, the coarse grains were replaced by ultrafine grains.

4.4 Mechanical properties and strengthening mechanisms

Figure 18(a) shows the mechanical property of the extruded and spun ZK61 tube tested along the AD with a strain rate of $1.0\times10^{-2}\,s^{-1}$ at room temperature. The extruded ZK61 tube exhibited

excellent strength with the yield stress and the ultimate strength of 226 and 303 MPa, respectively, and the elongation was 12.7%. After hot spinning, the yield stress increased to 243 MPa and the ultimate strength was improved to 334 MPa. Moreover, the elongation increased significantly up to 21.1%. Figure 18(b) exhibits the strain-hardening behavior of the ZK61 alloy. The hardening curves before and after hot spinning showed a similar feature. The strain hardening rate of the spun alloy was higher than that of the extruded alloy, and the decrease in the hardening rate after yielding was mainly attributed to slip-dominated softening [32]. WANG and CHOO [33] reported that the improvement in yield strength and plasticity was attributed to grain refinement according to the Hall−Petch relationship. After spinning, the GS reduction reached 71% and grain refinement could promote plastic deformation by coordinating more grains to participate in deformation. Moreover, the length of the dislocation slip was shortened and the dislocation pile-up at the grain boundary was released owing to grain refinement.

It was accepted that the modification of texture was important to the mechanical properties of Mg alloys. In this study, the texture of the spun ZK61 alloy with a strong preferential orientation was another important factor in strengthening the spun alloy. The improvement in yield strength could be achieved in Mg alloys with a strong basal texture by affecting the critical resolved shear stress (CRSS) ratios among slips and twinning. In the study of LOU et al [34], the textural hardening in yield strength was 10−45 MPa. Compared with the extruded ZK61 alloy, the random distribution of grain orientation in RD was greatly eliminated. Noteworthy, the tilt of the basal texture was related to the opening of the slip systems.

Figure 19 shows the grain orientation distribution of extruded and spun ZK61 alloy using crystal direction maps. The activation of different deformation mechanisms was dependent on the CRSS and Schmid factors. In Refs. [35,36], the main deformation mechanisms within the grains were tension twinning (θ=0°−23°, θ is the angle between the tension direction and c-axis), basal slip (θ=23°−77°) and prismatic slip (θ=77°−90°) when the CRSS ratio among basal slip, tension twinning and prismatic slip was 1:1:2 at room temperature. It was indicated that the activation fractions of different deformation mechanisms could be calculated based on the relationship between grain orientation and tension direction. The tension directions of the extruded and spun alloys were ED and AD (ED//AD). From Fig. 19(a), in the extruded fiber texture, the main deformation mechanism was prismatic slip (62.3%, in red) and basal slip was the second (37.3%, in green). Although the CRSS of prismatic slip was higher than that of basal slip, the Schmid factor of prismatic slip was much higher in the fiber texture, resulting in a higher activation fraction of prismatic slip. Since the c-axes of the grains were perpendicular to the tension direction, the tension twinning (in blue) was hard to activate when stretching along the ED. After spinning (Fig. 19(b)), the grain orientation slightly tilted to AD with an angle of 10°, which further restricted the activation of the basal slip. The fractions of basal slip declined to 29.4% and that of the prismatic slip increased to 69.8%. The texture alteration from extruded fiber texture to spun tilted plane texture further suppressed the basal slip.

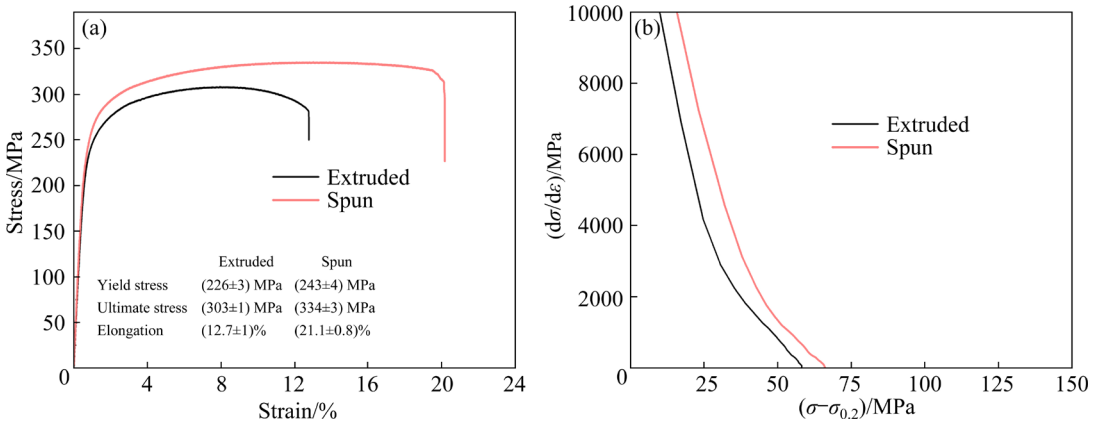

Fig. 18 Mechanical property of ZK61 tube: (a) Room temperature stress−strain curve before and after hot spinning; (b) Strain hardening curves

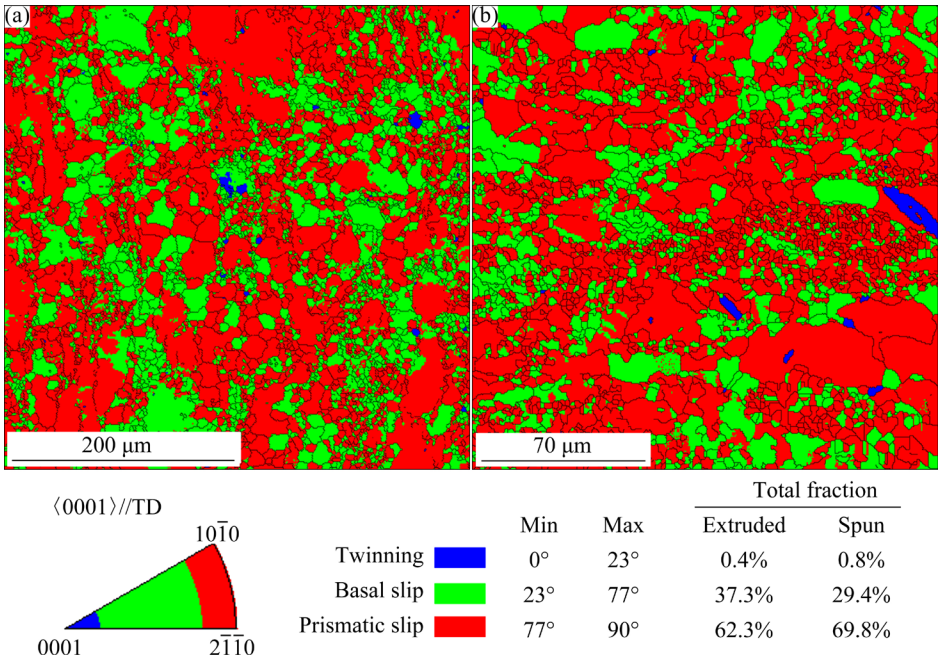

Fig. 19 Orientation distribution of ZK61 alloy after extrusion (a) and spinning (b) using crystal direction maps

Noted that the tension twinning was still hard to activate. Since the CRSS of prismatic slip was nearly twice as much as that of basal slip and tension twinning at room temperature, the activation of more prismatic slips needed higher external stress to coordinate plastic deformation, resulting in a higher stress. This was the reason why the texture modification of the spun ZK61 alloy exhibited higher yield stress.

5 Conclusions

(1) The unified ISV model was established including microstructural state variables during hot PSC. And the validation results showed that the ISV model could well predict the flow stress and the microstructure evolution.

(2) The ISV model was used in the hot spinning of ZK61 alloy via the FE software Abaqus and its subroutine Vumat. The simulated GS distribution and DRX fraction matched well with the experimental results under different hot spinning passes.

(3) After six passes of hot spinning, a tube with 1.4 mm in thickness was successfully fabricated. The yield strength improved from 226 to 243 MPa and the ultimate tensile strength increased from 303 to 334 MPa. Moreover, the fracture elongation significantly increased from 12.7% to 21.1%.

(4) The extruded (0002) fiber texture was replaced by (0002) plane texture after spinning which was slightly deflected in AD with an angle of ~10°. Moreover, the texture maximum intensity increased to 19.72.

(5) The formation of the ultrafine grains was attributed to the proliferation, movement and entanglement of dislocations during hot spinning. As the spinning proceeded, the dislocation density inside the dislocation wall increased and dislocation cells were formed, which further transformed into ultrafine grains.

CRediT authorship contribution statement

Jin-qi PAN: Conceptualization, Writing − Original draft, Formal analysis, Investigation, Methodology; **Wen-cong ZHANG:** Conceptualization, Formal analysis, Methodology; **Jian-lei YANG:** Conceptualization, Writing − Original draft, Formal analysis, Methodology; **Song-hui WANG:** Formal analysis, Investigation; **Yong WU:** Formal analysis, Methodology; **Huan LI:** Investigation.

Declaration of competing interest

The authors declare that they have no known competing financial interests or personal relationships that could have appeared to influence the work reported in this paper.

Acknowledgments

This work was supported by the National Natural Science Foundation of China (No. 51905123), Major Scientific and Technological Innovation Program of Shandong Province, China (Nos. 2020CXGC010303, 2022ZLGX04), and Key R&D Programme of Shandong Province, China (No. 2022JMRH0308).

References

[1] WANG Sen, LÜ Bin-Jiang, XU Tie-wei, CUI Ning, GUO Feng. Relationship between microstructure and mechanical properties of as-extruded and peak-aged Mg−6Al−3Sn−2Zn alloys [J]. Transactions of Nonferrous Metals Society of China, 2023, 33: 1385−1397.

[2] SOMEKAWA H, KINOSHITA A, WASHIO K, KATO A. Enhancement of room temperature stretch formability via grain boundary sliding in magnesium alloy [J]. Materials Science and Engineering A, 2016, 676: 427−433.

[3] JIANG Zhi-wei, YIN Dong-di, WAN You-fu, NI Ran, ZHOU Hao, ZHENG Jiang, WANG Qu-dong. Operating slip modes and inhomogeneous plastic deformation of Mg−10Gd−3Y−0.5Zr alloy during compression [J]. Transactions of Nonferrous Metals Society of China, 2023, 33: 79−94.

[4] GUO Rui, WANG Qiang, MENG Ying-ze, XU Wen-long, LI Guo-jun, ZHANG Zhi-ming, YU Hui-sheng, YU Jian-min. Compressive stress and shear stress on the deformation mechanism of Mg−13Gd−4Y−2Zn−0.5Zr alloy at different deformation temperatures [J]. Journal of Materials Research and Technology, 2022, 18: 1802−1821.

[5] WU Xiao-feng, XU Chun-xiang, ZHANG Zheng-wei, YANG Wen-fu, ZHANG Jing-shan. Microstructure evolution, strengthening mechanisms and deformation behavior of high-ductility Mg−3Zn−1Y−1Mn alloy at different extrusion temperatures [J]. Transactions of Nonferrous Metals Society of China, 2023, 33: 422−437.

[6] CHENG Wei-li, BAI Yang, MA Shi-chao, WANG Li-fei, WANG Hong-xia, YU Hui. Hot deformation behavior and workability characteristic of a fine-grained Mg−8Sn−2Zn−2Al alloy with processing map [J]. Journal of Materials Science & Technology, 2019, 35: 1198−1209.

[7] GAN Yi, HU Li, SHI Lai-xin, CHEN Qiang, LI Ming-ao, XIANG Lin, ZHOU Tao. Effect of AlLi phase on deformation behavior and dynamic recrystallization of Mg−Li alloy during hot compression [J]. Transactions of Nonferrous Metals Society of China, 2023, 33: 1373−1384.

[8] CAO Fu-rong, SUN Chao-feng, LIU Si-yuan, LIANG Jin-rui, LIU Ren-jia, GUO Hui-zhen, GUO Nan-pan. Microstructures, hot tensile deformation behavior and constitutive modeling in a superlight Mg−2.76Li−3Al−2.6Zn−0.39Y alloy [J]. Journal of Alloys and Compounds, 2022, 896: 163049.

[9] ZHANG Feng, LIU Zheng, WANG Yue, MAO Ping-lin, KUANG Xin-wen, ZHANG Zheng-lai, JU Ying-dong, XU Xiao-zhong. The modified temperature term on Johnson−Cook constitutive model of AZ31 magnesium alloy with {0002} texture [J]. Journal of Magnesium and Alloys, 2020, 8: 172−183.

[10] XIA Xian-sheng, CHEN Qiang, ZHANG Kui, ZHAO Zu-de, MA Ming-long, LI Xing-gang, LI Yong-jun. Hot deformation behavior and processing map of coarse-grained Mg−Gd−Y−Nd−Zr alloy [J]. Materials Science and Engineering A, 2013, 587: 283−290.

[11] HUO Yuan-ming, BAI Qian, WANG Bao-yu, LIN Jian-guo, ZHOU Jing. A new application of unified constitutive equations for cross wedge rolling of a high-speed railway axle steel [J]. Journal of Materials Processing Technology, 2015, 223: 274−283.

[12] ALABORT E, PUTMAN D, REED R C. Superplasticity in Ti−6Al−4V: Characterisation, modelling and applications [J]. Acta Materialia, 2015, 95: 428−442.

[13] XU Wen-chen, YUAN Can, WU He, YANG Zhong-zhe, YANG Guo-jing, SHAN De-bin, GUO Bin, JIN Bo-cheng. Modeling of flow behavior and microstructure evolution for Mg−6Gd−5Y−0.3Zr alloy during hot deformation using a unified internal state variable method [J]. Journal of Materials Research and Technology, 2020, 9: 7669−7685.

[14] SU Ze-xing, SUN Chao-yang, WANG Ming-jia, QIAN Ling-yun, LI Xin-tong. Modeling of microstructure evolution of AZ80 magnesium alloy during hot working process using a unified internal state variable method [J]. Journal of Magnesium and Alloys, 2022, 10: 281−294.

[15] JIN Xue-ze, XU Wen-chen, YANG Guo-jing, SHAN De-bin, GUO Bin. Microstructure evolution and strengthening mechanisms of Mg−6Gd−4Y−0.5Zn−0.5Zr alloy during hot spinning and aging treatment [J]. Materials Science and Engineering A, 2021, 827: 142035.

[16] CAO Zhen, WANG Feng-hua, WAN Qu, ZHANG Zhen-yan, JIN Li, DONG Jie. Microstructure and mechanical properties of AZ80 magnesium alloy tube fabricated by hot flow forming [J]. Materials & Design, 2015, 67: 64−71.

[17] YASMEEN T, SHAO Zhu-tao, ZHAO Lei, GAO P, LIN Jian-guo, JIANG Jun. Constitutive modelling for the simulation of the superplastic forming of TA15 titanium alloy [J]. International Journal of Mechanical Sciences, 2019, 164: 105178.

[18] LIN J G. Fundamentals of materials modelling for metals processing technologies: Theories and applications [M]. World Scientific Publishing Co Inc, 2015.

[19] YU Zi-jian, XU Chao, MENG Jian, ZHANG Xu-hu, KAMADO S. Microstructure evolution and mechanical properties of as-extruded Mg−Gd−Y−Zr alloy with Zn and Nd additions [J]. Materials Science and Engineering A, 2018, 713: 234−243.

[20] LIN J, LIU Y, FARRUGIA D C J, ZHOU M. Development of dislocation-based unified material model for simulating microstructure evolution in multipass hot rolling [J]. Philosophical Magazine, 2005, 85:1967−1987.

[21] LIN J, DEAN T A. Modelling of microstructure evolution in hot forming using unified constitutive equations [J]. Journal of Materials Processing Technology, 2005, 167: 354−362.

[22] JI Hong-chao, LIU Jin-ping, WANG Bao-yu, TANG Xue-feng, LIN Jian-guo, HUO Yuan-ming. Microstructure evolution and constitutive equations for the high-temperature deformation of 5Cr21Mn9Ni4N heat-resistant steel [J]. Journal of Alloys and Compounds, 2017, 693: 674−687.

[23] CHO H E, HAMMI Y, BOWMAN A L, KARATO S I,

BAUMGARDNER J R, HORSTEMEYER M F. A unified static and dynamic recrystallization internal state variable (ISV) constitutive model coupled with grain size evolution for metals and mineral aggregates [J]. International Journal of Plasticity, 2019, 112: 123−157.

[24] SANDSTOM R, LAGNEBORG R. A model for hot working occurring by recrystallization [J]. Acta Metallurgica, 1975, 23: 387−398.

[25] LIN J, LIU Y. A set of unified constitutive equations for modelling microstructure evolution in hot deformation [J]. Journal of Materials Processing Technology, 2003, 143−144.

[26] MOHAMED M, FOSTER A, LIN J, BALINT D, DEAN T. Investigation of deformation and failure features of AA6082: experimentation and modelling [J]. International Journal of Machine Tools & Manufacture, 2011, 53: 27−38.

[27] LANGKRUIS V D, LOF J, KOOL W H, ZWAAG V D, HUETINK J. Comparison of experimental AA6063 extrusion trials to 3D numerical simulations using a general solute-dependent constitutive model [J]. Computational Materials Science, 2000, 18: 381−392.

[28] ARENTOFT M, GRONOSTAJSKI Z, NIECHAJOWICZ A, WANHEIM T. Physical and mathematical modelling of extrusion processes [J]. Journal of Materials Processing Technology, 2000, 106: 2−7.

[29] XIA Qin-xiang, LONG Jin-chuan, XIAO Gang-feng, YUAN Shuai, QIN Yi. Deformation mechanism of ZK61 magnesium alloy cylindrical parts with longitudinal inner ribs during hot backward flow forming [J]. Journal of Materials Processing Technology, 2021, 296: 117197.

[30] LEI Wei-wei, ZHANG Hui. Analysis of microstructural evolution and compressive properties for pure Mg after room-temperature ECAP [J]. Materials Letter, 2020, 271: 127781.

[31] SUN Chao, LIU Huan, WANG Ce, Ju Jia, WANG Guo-wei, JIANG Jing-hua, MA Ai-bin, BAI Jing, XUE Feng, XIN Yun-chang. Anisotropy investigation of an ECAP-processed Mg−Al−Ca−Mn alloy with synergistically enhanced mechanical properties and corrosion resistance [J]. Journal of Alloys and Compounds, 2022, 911: 165046.

[32] ZHANG Li-xin, CHEN Wen-zhen, ZHANG Wen-cong, WANG Wen-ke, WANG Er-de. Microstructure and mechanical properties of thin ZK61 magnesium alloy sheets by extrusion and multi-pass rolling with lowered temperature [J]. Journal of Materials Processing Technology, 2016, 237: 65−74.

[33] WANG Yi, CHOO H. Influence of texture on Hall−Petch relationships in an Mg alloy [J]. Acta Materials, 2014, 81: 83−97.

[34] LUO X Y, LI M, BOGER R K, AGNEW S R, WAGONER R H. Hardening evolution of AZ31B Mg sheet [J]. International Journal of Plasticity, 2007, 23: 44−86.

[35] GUAN Bo, XIN Yun-chang, HUANG Xiao-xu, WU Pei-dong, LIU Qing. Quantitative prediction of texture effect on Hall−Petch slope for magnesium alloys [J]. Acta Materials, 2019, 173: 142−152.

[36] YU Hui-hui, XIN Yun-chang, WANG Mao-yin, LIU Qing. Hall−Petch relationship in Mg alloys: A review [J]. Journal of Materials Science & Technology, 2018, 34: 248−256.

采用统一粘塑性本构模型预测 ZK61 镁合金热旋压过程中的显微组织演变

潘金启[1]，张文丛[1]，杨建雷[1]，王松辉[1]，武 永[2]，李 焕[1]

1. 哈尔滨工业大学(威海) 材料科学与工程学院，威海 264209；
2. 南京航空航天大学 机电工程学院，南京 210016

摘 要：基于高温平面应变压缩实验结果建立了统一粘塑性本构模型用以预测 ZK61 镁合金热旋压过程中的组织演变过程。统一粘塑性本构模型考虑了各种内变量参数的影响并且使用遗传算法对各参数进行了优化计算，随后利用 Vumat 子程序定义材料属性并嵌入 Abaqus 有限元热旋压仿真模型中，对材料的晶粒尺寸和再结晶分数进行预测。结合热旋压仿真结果和实验结果，证明了统一粘塑性本构模型对材料旋压过程中的组织演变具有良好的可预测性。由于动态再结晶细晶强化和织构强化作用，旋压后的 ZK61 合金薄壁筒形件强度从 303 MPa 提升至 334 MPa；并且，在旋压组织中发现了平均晶粒尺寸为 0.5 μm 的超细晶，这些超细晶是由于旋压成形中位错的增殖、运动和缠结产生的，对材料的强度具有重要的影响。

关键词：统一粘塑性本构模型；热旋压；ZK61 合金；有限元仿真；织构演变

(Edited by Bing YANG)